Machine Learning for Identifying Dynamical Phases in Topological Lasers

Stephan Wong, Doris E. Reiter, and Sang Soon Oh

Abstract Identifying phases and analyzing the stability of dynamic states are common and important problems that appear in a variety of physical systems. However, drawing a phase diagram in high-dimensional and large parameter spaces has proven to be challenging. In this chapter, we will look at a data-driven method to obtain the phase diagram of lasing modes in photonic topological insulator lasers. The classification is based on the temporal behaviour of the topological modes obtained via numerical integration of the rate equation. An unsupervised learning method is used and an adaptive library is constructed in order to distinguish the different topological modes present in the generated parameter space. We start by introducing photonic topological lasers and Su-Schrieffer-Heeger lattices with saturable gain. Then, we look at different dynamic mode decomposition methods for a parameter space defined as the gain and loss parameters. Finally, we classify the topological phases of the topological lasing modes using the library automatically determined by top-down and bottom-up classification approaches.

1 Introduction

A laser is a light emitting device composed of an optical resonator, called optical cavity, and gain medium which provides optical gain. Nowadays lasers are widely used in our life as well as in various fields of scientific research. The optical cavities of those lasers are made up of one optical resonator or an array of coupled optical

---

S. Wong (✉)
Center for Integrated Nanotechnologies, Sandia National Laboratories, Albuquerque, NM, USA
e-mail: stephan_wong@hotmail.fr

D. E. Reiter
Condensed Matter Theory, TU Dortmund University, Dortmund, Germany
e-mail: doris.reiter@tu-dortmund.de

S. S. Oh
School of Physics and Astronomy, Cardiff University, Cardiff, UK
e-mail: ohs2@cardiff.ac.uk

M. te Vrugt (ed.), *Artificial Intelligence and Intelligent Matter*, Machine Intelligence
for Materials Science, https://doi.org/10.1007/978-3-032-04129-6_9

resonators. The laser is referred to as a photonic topological insulator (PTI) laser when the optical resonators are coupled to each other to form a topological insulator and lase with topological modes. They are also called topological lasers. These PTI lasers are particularly interesting because they can lase with topological edge modes [1] or corner modes [2] which are robust to structural defects and show phase-locking between the optical resonators. Therefore, significant research efforts have been made on PTI lasers especially focusing on spatial stability, i.e., the robustness of lasing modes to geometrical defects. However, lasers are open systems and thus non-Hermitian systems in which energy is exchanged with the surrounding external systems making the lasing modes dynamic with time-varying optical fields and carrier populations. Moreover, they are nonlinear due to the optical gain that depends on the mode intensities and complex light-matter interactions in the gain medium. Consequently, without taking into account their dynamic nature, a description of lasing is incomplete.

To explore the dynamics and temporal stability of lasing modes, one can use the linear stability analysis to solutions of coupled rate equations [3]. However, it becomes challenging when we apply it to more complex systems such as lasing modes in coupled lasers. This is because the analytical approach easily fails due to the lack of analytical solutions for high-dimensional parameter space and the emergence of complex and diverse dynamic phases [4]. Yet, numerical methods can offer solutions for the coupled rate equations enabling us to classify the lasing modes based on simulation results. For a high-dimensional and large parameter space, however, the simulation can be very costly and drawing the phase diagram is not a straightforward task. It is even more challenging when we do not know all the possible phases present in the laser system. Unfortunately, this is true for most of dynamic systems in nature.

Machine learning (ML) can be advantageous in tackling such problems that require repeated numerical simulations, since it can significantly reduce the number of simulations. Depending on the type of dataset, i.e., whether the data are labelled or not, different strategies of ML can be used: a supervised learning and an unsupervised learning. On one hand, the supervised learning strategy relies on labelled data, a dataset of input-output pairs. This strategy has been utilized in topological photonics [5] to draw topological phase diagrams [6], calculate topological invariants [7], or explore topological band structures [8]. On the other hand, in the unsupervised learning strategy, we extract information from the dataset which does not have labels. This strategy is useful for dimensional reductions which keep only the main features of the high-dimensional structure of the dataset, or for clustering problems where the data is classified into different types [9]. For instance, this has been successful in obtaining the phase transition in the Ising model [10], and clustering Hamiltonians that belong to the same symmetry classes [11].

In this chapter, we introduce a representation classification method to study the spatio-temporal dynamics of nonlinear topological systems. The results will be analyzed based on the phase diagram of the Su-Schrieffer-Heeger (SSH) lattice [12] with a domain wall and with saturable gain [4, 13]. Without involving any detailed knowledge on the complex system, the algorithm constructs an appropriate library of the different phases automatically. To build the library, we will employ two approaches:

a top-down approach in which the library has numerous phases that are merged into the equivalent phases, and a bottom-up approach in which the library is constructed on the fly to obtain the most accurate classification.

2 Physics of Photonic Topological Insulator Lasers

The field of PTI lasers has sparked interest since the first topological lasers were demonstrated [1, 14], resulting in a great success story [15–17]. While we refer to recent overview articles on the latest developments on PTI lasers [18, 19], we here briefly highlight the main concepts of a PTI laser.

2.1 A Brief Introduction to Photonic Topological Insulator Lasers

PTI lasers combine the advantages of topological photonics with laser physics by an optical cavity designed with a topological array. A topological array or a topological insulator is a special photonic crystal structure that features unique edge modes that are topologically protected. Such edge modes form when combining two materials that differ in their properties regarding their wave function, mostly quantified by a winding number. The topological array can be one-dimensional (1D) or two-dimensional (2D) and the arrangement can be of different types depending on how different coupling coefficients are arranged.

The 2D photonic topological structures are interesting because it is possible to create waveguides which guide the light without losses in arbitrary paths, in particular around edges. In contrast, a perfect bending of light is not possible in conventional waveguides, where bending always leads to scattering losses. Designing such topological waveguides is achieved by topological edge modes. Examples of 2D photonic topological structures are the perturbed honeycomb lattice [21] and the perturbed kagome lattice [16]. The honeycomb lattice features a photonic Dirac cone, but when slightly distorted, i.e., when the hexagons are stretched or compressed, bands with distinct topologies appear [21]. Combining a stretched with a compressed honeycomb lattice results in the occurrence of topological modes at the interface. The topological modes are topologically protected and as such also robust against defects and disorders.

Examples of 2D photonic structures are shown in Fig. 1. In Fig. 1a, a combination of a compressed Kagome lattice (upper part in red) and a stretched Kagome lattice (lower part, blue) are shown. Then, a topological edge mode is formed at the interface between the two parts which due to construction has sharply curved corners. In the lower panel the light field amplitude of the edge mode travelling along the interface is displayed. Due to its spatial symmetry, bending the light is possible without scat-

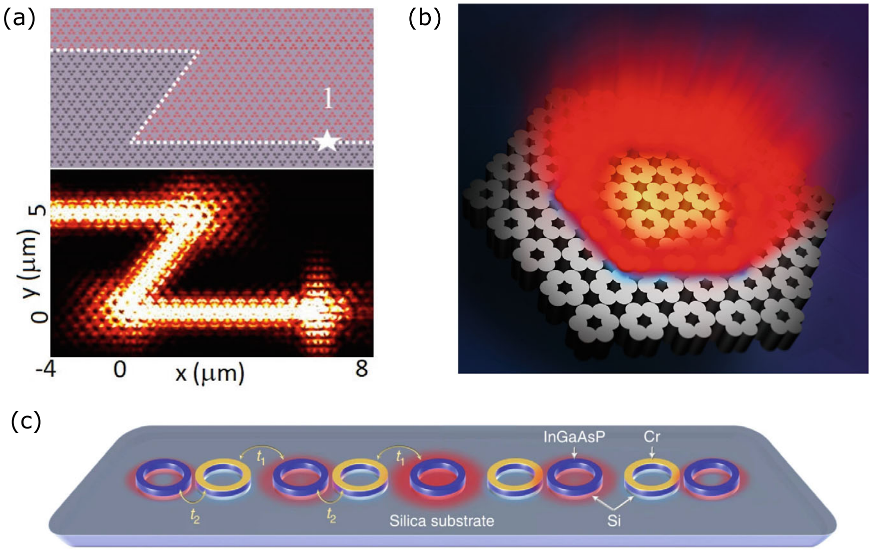

Fig. 1 **Structures for PTI lasers**: **a** A combination of two Kagome lattices supporting a topological edge mode between them. Light can travel along the edge mode with minimal losses, even though there exist strong bendings as shown in the simulated electric field. Kagome lattices can be used for PTI lasers. Reprinted (adapted) with permission from [16]. Copyright 2020 American Chemical Society. All Rights Reserved. **b** Artistic view of two honeycomb lattices featuring an edge mode between them. Each site is a VCSEL made from semiconductor nanostructures. Due to their arrangements, the VCSELs lase into the topological mode, forming a PTI laser. Figure provided by Sebastian Klembt, a similar figure can be found in Ref. [17]. **c** Schematic of a one-dimensional topological array on a hybrid silicon platform. Each ring is a nanostructure of InGaAsP quantum well layers on top of silicon. Every other ring has an additional layer of Cr. This structure is an implementation of the 1D-SSH model. Figure reproduced from [20], published under a CC BY 4.0 license

tering and reflection losses, which in a regular waveguide would be associated with significant losses [16].

In a PTI laser, topological edge modes or topological cavities are combined with lasing materials to make use of the great advantage of photonic topological modes. Figure 1b shows a PTI laser based on the deformed honeycomb lattice. In the outer part the hexagons are compressed, in the inner part the hexagons are stretched. Each site is a vertical microcavity featuring a gain medium between distributed Bragg mirrors, thus, forming a vertical-cavity surface-emitting laser (VCSEL). When pumped, in total 30 of the VCSEL structures lase coherently into the topological mode [17].

PTI lasers also exists in 1D, as shown in Fig. 1c. The lattice is now formed by the combination of two nano-rings, each composed of a layered semiconductor structure. Every other ring has an additional Cr layer. On the right and left side the arrangement changes, such that in the center a topological mode is formed, which can feature lasing. This 1D structure is interesting, because it is a realization of the SSH model [20], which is a well-established theoretical model in the condensed matter physics.

2.2 Su-Schrieffer-Heeger Model for PTI Lasing

The SSH model describes a one-dimensional chain lattice with topological features [12]. Originally it was derived to describe electrical conductivity and soliton physics, while nowadays it is a standard model in topological photonics. A sketch of the SSH lattice is shown in Fig. 2a. Two lattice sites A and B form the unit cell. Within that unit cell the sites are coupled via the parameter t_1, while the coupling between unit cells is given by the parameter t_2. In the center, the lattice changes and accordingly a topological mode is formed.

To include lasing in the SSH model, at each site n a linear gain g_n and a linear loss γ_n is introduced. This leads to a dynamics at each lattice site, which can be described by solving the equations of motion

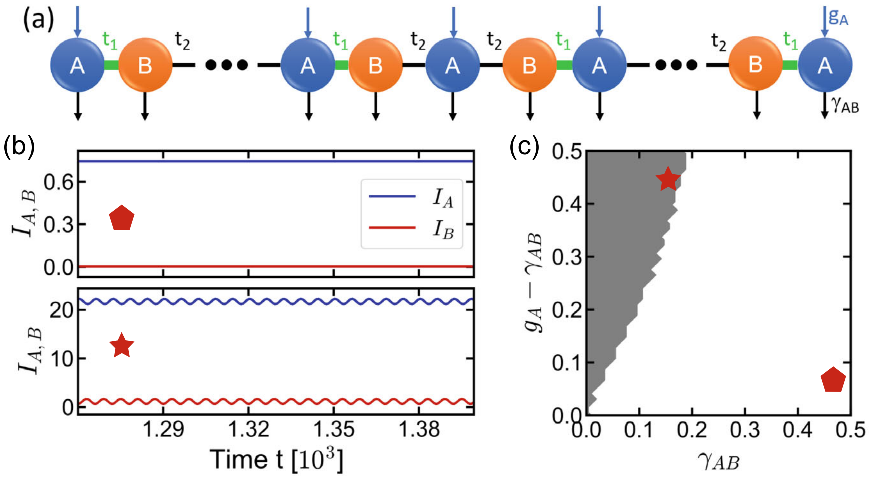

Fig. 2 Phase diagram of the domain-wall-type Su-Schrieffer-Heeger (SSH) lattice with saturable gain. a Sketch of the SSH lattice feature unit cells composed of site A and site B. The coupling within the unit cell is of strength t_1 and between cells t_2. In the center the lattice changes leading to a topological mode. To introduce lasing, gain of the strength g_A acts on each site A and losses γ_{AB} act on all lattice sites. **b** Representative time-evolution of the total intensity I_A (and I_B) of the A (and B) sublattice for the non-oscillating (top) and oscillating (bottom) topological lasing mode. **c** Phase diagram of the SSH lattice shown in panel (a). The red pentagon and star mark the parameter space position of the time-evolutions plotted in panel (b). The oscillating (red star) and non-oscillating (red pentagon) topological modes displayed are chosen at $(\gamma_{AB}, g_A - \gamma_{AB}) = (0.16, 0.44)$ and $(0.48, 0.06)$, respectively

$$i\frac{da_p}{dt} = i\left(\frac{g_A}{1+|a_p|^2} - \gamma_A\right)a_p + t_{1,2}b_p + t_{2,1}b_{p-1}, \tag{1}$$

$$i\frac{db_p}{dt} = i\left(\frac{g_B}{1+|b_p|^2} - \gamma_B\right)b_p + t_{1,2}a_p + t_{2,1}a_{p+1}, \tag{2}$$

where a_p and b_p are respectively the amplitudes of the A and B sites on the p-th unit cell, g_σ and γ_σ are the linear gain and linear loss at the site $\sigma = A, B$, and the couplings $t_{1,2}$ (and $t_{2,1}$) are either t_1 or t_2 (and t_2 or t_1) depending on the lattice sites [see Fig. 2a]. If the dynamics is coherent, lasing occurs. We quantify this by considering the dynamics of the amplitude I_A of the sum of all lattice sites A (and I_B respectively).

In our calculations, we set the gain just to occur at the A sites with g_A, while the gain at all B sites is zero $g_B = 0$. The losses are assumed to be the same for all sites with $\gamma_A = \gamma_B = \gamma_{AB}$, as in Refs. [4, 13]. We take a lattice consisting of $N_s = 21$ sites. Depending on the parameters, we can find two different behaviours/modes as shown in Fig. 2b: In the non-oscillating mode (top) the amplitudes $I_{A,B}$ stay constant for all times and no dynamics occurs. In the oscillating mode (bottom), the amplitudes $I_{A,B}$ oscillate in a steady state.

The parameters to distinguish between the modes are given in the phase diagram shown in Fig. 2c with the examples in Fig. 2b marked by red symbols. For one-dimensional cases like the SSH model with gain/loss, the equations of motion can be solved and the phase diagram can be calculated exactly. However, as soon as we consider higher dimensions obtaining the phase diagram is not as simple and new methods have to be sought.

In the following, we will thus explore whether ML learning techniques are helpful to draw the phase diagram of the PTI laser. For this, we need to classify the dynamical behaviour of the lasing modes. The solutions presented in Fig. 2c, from Ref. [4], will act as a benchmark for the ML results, by showing the shaded areas in our results.

3 Dynamical Behavior Identified by Representation Classification

Given a set of samples with unknown dynamical behaviors, we aim to identify their dynamical behaviors using representation classification. The fundamental idea of the representation classification method consists of identifying the samples based on a constructed library $\mathcal{L}$. The manual construction of the library constitutes the supervised learning part of the representation classification method where the dynamical behaviors of interest are utilized to construct the library for subsequent identification of their dynamics. Figure 3 shows the outcomes of this classification method. While it fails to correctly reproduce the phase diagram in the literature [4], leveraging the supervised learning part in an adaptive construction of the library gives more reasonable results [22], as we will see later in this chapter.

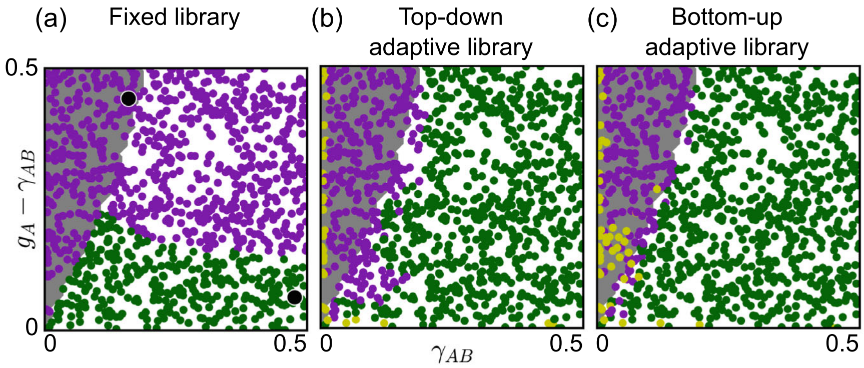

Fig. 3 **Outcome of the representation classification**. Phase diagram obtained with representation classification (**a**) from a fixed library composed two regimes (one oscillating and one non-oscillating), **b** from a top-down adaptive library, **c** from a bottom-up adaptive library. The purple, green and yellow dots correspond respectively to the identified oscillating, non-oscillating and transient regimes. The black dots represent the regimes used for the construction of the library. The fixed library is composed of the black dots located at $(\gamma_{AB}, g_A - \gamma_{AB}) = (0.48, 0.06)$ and $(0.16, 0.44)$, γ_{AB} and g_A are, respectively, the linear loss and gain on the A sites. The white and grey areas are overlays of the referenced phase diagram obtained in Fig. 2

The process of constructing the library $\mathcal{L}$ in the representation classification method relies on the dynamical behaviors we want to identify. If we assume that the dynamical behavior of the topological laser evolves on a low D-dimensional attractor, meaning that the system will behave the same over time once the transient is passed, then the underlying behaviors of the system can be accurately approximated by a reduced-order model. In particular, this means that the dynamics of the system can be described by a low D-dimensional vector space, where the basis vectors $\Phi = \{\phi_i\}_{i=1,\dots,D}$ are used to approximate the system's spatio-temporal dynamics $x(t)$ (or the measured state at time t) close to the attractor as:

$$x(t) \approx x_D(t) := \sum_{i=1}^{D} \phi_i \beta_i(t) = \Phi\beta(t) \tag{3}$$

where β_i are the weighted coefficients in the above linear combination of basis states ϕ_i. The library will therefore be composed of the bases representing each nonlinear regime of interest in order to identify the dynamical regimes of each samples, namely to classify the samples into different phases. Specifically, the library $\mathcal{L}$ is a set of bases each of them spanning the appropriate desired dynamical behaviors:

$$\mathcal{L} = \{\Phi_1, \dots, \Phi_J\} = \{\phi_{j,i}\}_{j=1,\dots,J\,,\, i=1,\dots,D}, \tag{4}$$

where J is the number of regimes, Φ_j are the bases of each of the dynamical regime j, and $\phi_{j,i}$ are the corresponding basis states. Therefore, the spatio-temporal dynamics $x(t)$ can now be approximated as:

$$x(t) \approx x_{_{JD}}(t) := \sum_{j=1}^{J} \sum_{i=1}^{D} \phi_{j,i} \beta_{j,i}(t) = \sum_{j=1}^{J} \Phi_j \beta_j(t) \tag{5}$$

where $\beta_{j,i}$ are coefficients corresponding to the contributions of the dynamical regimes in the library.

The dynamical regime of each sample is identified by finding the basis with the highest contribution to the approximated reconstruction dynamics [Eq. (5)]. More precisely, the classification strategy consist of finding the vector space within each dynamics in the library that has the highest projection measurement at a particular time t_i (or time window $[t_i : t_{i+N_w}]$):

$$j^* = \arg \max_{j=1,\dots,J} \| P_j x(t_i : t_{i+N_w}) \|_2, \tag{6}$$

where $x(t_i : t_{i+N_w})$ is the notation for the state measured within the time window $[t_i, t_{i+N_w}]$ with N_w the time step window size, namely the vector $[x(t_i), \dots, x(t_{i+N_w})]$, and P_j is the projection operator onto the bases of the regime j in the library $\mathcal{L}$:

$$P_j = \Phi_j \Phi_j^+ \tag{7}$$

with Φ_j^+ being the pseudo-inverse of Φ_j. In Eq. (6), $\|\cdot\|_2$ is the ℓ^2-norm of a vector defined as $\|v\|_2 := \sqrt{\sum_i |v_i|^2}$, and arg max is the function that returns the index corresponding to the maximum value.

3.1 Decomposition Method

The basis vectors Φ_j approximating the dynamical regime j can be found via different decomposition methods. Depending on the decomposition methods, the classification will yield different results as it focuses on different features (see Fig. 4). In this section, three methods will be covered with an highlight on the features translated into the bases: The proper orthogonal decomposition (POD), the dynamical mode decomposition (DMD), and the augmented dynamical mode decomposition (aDMD).

Common to all the decomposition methods is the use of the data matrix X built from the dynamical data at hand. The data matrix is a $(N_s \times N_t)$-matrix that gathers the N_t data snapshots $x(t_i)$ into columns:

$$X = \left[(t_1), \dots, x(t_{N_t})\right]. \tag{8}$$

Here, N_s is the number of sites in the system, namely $N_s = 21$. In the remaining of the chapter, the vectors $x(t_i)$ are chosen to be the complex-valued amplitudes of the modes at the A and B sites. Exploring alternative "observables", such as the absolute values or the total intensities per sublattice, is reserved for a future investigation and is beyond the scope of this chapter.

3.1.1 Proper Orthogonal Decomposition

The proper orthogonal decomposition (POD) [23] method is a common decomposition method based on the singular value decomposition (SVD) of the data matrix.

The data matrix is first decomposed via SVD:

$$X = U \Sigma V^{\dagger} \tag{9}$$

where U and $V^{\dagger}$ are $(N_s \times N)$ and $(N \times N_t)$ unitary matrices, respectively, and Σ is a diagonal $(N \times N)$-matrix $\mathrm{diag}(\sigma_1, \ldots, \sigma_N)$, with $N = \min(N_s, N_t)$. The diagonal entries of Σ are the so-called singular values, and are ordered in ascending order $\sigma_1 > \sigma_2 > \ldots > \sigma_N \geq 0$. Because the singular values can be obtained from the eigenvalue of XX^T, they can be interpreted as the variance of the data matrix. The columns of U, called the singular vectors, are thus ordered according to the variance σ_i they capture in the data matrix.

Intuitively, the POD method can be seen as performing a space-time separation of the data matrix as the SVD of X can explicitly be written as:

$$X_{im} = \sum_{n=1}^{N} U_{in} \sigma_n V^{\dagger}_{nm}, \tag{10}$$

where the columns of U contain the spatial information, while the rows of $V^{\dagger}$ have the temporal information at each spatial grid point.

The POD method consists of choosing the singular vectors, also called the POD modes, as being the basis Φ_j used for approximating the spatio-temporal dynamics. Yet, given the data matrix is typically large, the resulting size of the POD basis is correspondingly large as well, making the computation of the projector in the classification [Eq. (7)] impractical. To reduce the number of basis vectors used to approximate the dynamics, the POD basis U is truncated according to a cut-off value r while retaining the main information of the data matrix. More precisely, this is realized by keeping only the r highest terms in the decomposition [Eq. (10)], namely by keeping the POD modes with the r highest variance they capture in the data matrix X:

$$X_{im} \simeq \sum_{n=1}^{r} U_{in} \sigma_n V^{\dagger}_{nm}. \tag{11}$$

In a matrix form, the truncation reads:

$$X \simeq U_r \Sigma_r V_r^\dagger, \tag{12}$$

where U_r, Σ_r and $V_r^\dagger$ are the truncated matrix of U, Σ and $V^\dagger$, respectively. Although the cut-off value r can be chosen based on different criteria [24], r implicitly depends on the dimension of the vector space needed to approximate the attractor and is typically chosen so that the POD modes retain a certain amount of the variance σ_X in the data, namely:

$$\sum_{n=1}^{r} \sigma_i > \sigma_X. \tag{13}$$

The vectors used to build the basis Φ_j are therefore the reduced POD basis, namely $\Phi_j^{(\mathrm{POD})} = U_r$.

However, the POD modes represent a static picture of dynamics and do not explicitly model the temporal dynamics of the time series. This method will therefore most likely fail to identify the correct dynamical regime in the classification step [see discussion in Sect. 3.2]. Nonetheless, for didactic purposes, it is important to introduce this concept.

3.1.2 Dynamical Mode Decomposition

The dynamical mode decomposition (DMD) [23, 25, 26] method is an alternative to the POD method for learning the dynamics of nonlinear systems.

Indeed, the DMD method can extract the spatio-temporal patterns of the data matrix by considering the linear mapping, namely the matrix A, between the dynamics starting at time t_1 and at time t_2. Explicitly, the linear mapping A is defined by

$$X_2 = AX_1, \tag{14}$$

where X_1 is the data matrix starting at some time steps t_1, and X_2 is the data matrix starting at the next time step t_2, namely:

$$X_1 = \left[x(t_1), x(t_2), \dots, x(t_{N_t-1})\right] \tag{15}$$

and

$$X_2 = \left[x(t_2), x(t_3), \dots, x(t_{N_t})\right]. \tag{16}$$

The definition of the matrix A [Eq. (14)] is similar to the equation for a linear stability analysis of discrete maps. Solving the eigenvalue problem for the matrix A will therefore give us information about both the spatial profiles and the temporal evolutions with its eigenvectors and eigenvalues, respectively. In particular, if the eigenvalue problem is written as:

$$A\Psi = \Psi\Lambda \tag{17}$$

where the columns of Ψ are called the DMD modes ψ_i and the corresponding DMD eigenvalues λ_i are the diagonal entry of Λ, then the DMD modes ψ_i give us the spatial profile of the eigenmodes while their corresponding eigenvalues λ_i have their temporal information. Because the DMD eigenvalues λ_i are eigenvalues of an evolution operator, they are of the form $\lambda_i = e^{\Omega_i \Delta t}$, with $\Delta t = t_2 - t_1$. The temporal evolution quantities of interest are thus given by Ω_i:

$$\Omega_i = \frac{\ln(\lambda_i)}{\Delta t} = i\omega_i + \mu_i \tag{18}$$

where ω_i is the oscillation frequency of the DMD modes ψ_i, and μ_i is its growth (or decay) rate if $\mu_i > 0$ (or $\mu_i < 0$).

At its core, the DMD method decomposes the data into a set of coupled spatio-temporal modes. Conceptually, the DMD combines the POD method in the spatial domain with the discrete Fourier transform in the time domain for the oscillating behavior. Notably, DMD goes even beyond these comparisons by additionally providing an estimation of the growth (or decay) rate in time via $\mu_i > 0$ (or $\mu_i < 0$).

In the DMD method, the basis vectors used for the construction of the library $\mathcal{L}$ are the DMD modes Ψ. However, the eigendecomposition is not feasible by direct computation as the size of the matrix A is typically large, and all the DMD modes are not needed for similar reasons to the POD method. Instead, the DMD modes and eigenvalues can be obtained via the truncated data matrices of X_1 and X_2. The algorithm starts with the truncated SVD of $X_1 \approx U_r \Sigma_r V_r^\dagger$ in which Eq. (14) becomes:

$$X_2 \approx A U_r \Sigma_r V_r^\dagger. \tag{19}$$

The matrix A is then projected onto the truncated POD subspace:

$$A_r := U_r^\dagger A U_r \approx U_r^\dagger X_2 V_r \Sigma_r^{-1}. \tag{20}$$

The eigenvalue problem for A_r is solved with:

$$A_r W = W\Lambda, \tag{21}$$

from which the truncated DMD modes can now be written as [27]:

$$\Psi_r = X_2 V_r \Sigma_r^{-1} W, \tag{22}$$

and still approximately satisfy the relation in Eq. (17). The basis vectors used in the library construction are therefore $\Phi_j^{(\mathrm{DMD})} = \Psi_r$.

Nevertheless, it is the DMD eigenvalues λ_i that carry the temporal information. Akin to the POD method, the DMD basis captures only the spatial information, leading outcomes comparable to those of the POD method [see discussion in Sect. 3.2].

3.1.3 Time-Augmented Dynamical Mode Decomposition

The time-augmented DMD (aDMD) consists in incorporating the temporal information into the DMD basis [28].

Indeed, although the DMD captures the temporal evolution of the dynamics, the temporal information is not directly incorporated in the DMD modes used for constructing the basis of the attractor's vector space. Instead, the set of vectors $\{(\psi_{r,i}), (\lambda_i \psi_{r,i}), (\lambda_i^2 \psi_{r,i}), \ldots, (\lambda_i^{N_w} \psi_{r,i})\}$ gives an idea of the evolution of the DMD mode $\psi_{r,i}$, as λ_i is similar to a time-evolution operator, i.e., multiplying by λ_i is equivalent to shifting by one time step. The temporal information is therefore included in the DMD by constructing a time-augmented basis [28]:

$$\psi_{r,i}^{(N_w)} = \begin{bmatrix} \psi_{r,i} \\ \lambda_i \psi_{r,i} \\ \vdots \\ \lambda_i^{N_w} \psi_{r,i} \end{bmatrix}. \tag{23}$$

Because the time-augmented vectors Eq. (23) exhibit the time-evolution of the DMD vectors, these vectors constitute the basis used for constructing the library $\mathcal{L}$, namely $\Phi_j^{(\text{aDMD})} = \Psi_{r,i}^{(N_w)}$, with $\Psi_{r,i}^{(N_w)} = [\psi_{r,1}^{(N_w)}, \psi_{r,2}^{(N_w)}, \ldots]$.

The identification is now slightly different than for the POD and DMD, as the projection measurement is realized over a time window $[t_i, t_i + N_w]$, as shown in Eq. (6). In consequence, the outcome of the aDMD method gives now better results, even though this is far from being accurate as we will see in the next section.

3.2 *Classification*

After acquiring the basis composing the library $\mathcal{L}$, we can now proceed with classifying the samples using the basis derived from the representative dynamics. The representative dynamics are here randomly chosen within each known dynamical phases, namely the oscillating and non-oscillating modes [see Fig. 2], and they are depicted by the black dots in Fig. 4. In order to avoid the transient regime and to get closer to the attractor's dynamics, the bases are constructed from the time series after starting at the 1800-th time step.

The phase diagram results from the identification of the sample with respect to the representative dynamics as shown in Eq. (6). In the phase diagrams, we color-coded the different identified regimes, where the purple (and pink) dots always mark the oscillating regime, and the green dots the non-oscillating regime. As we will see later, the yellow dots correspond to the transient regime and the orange dots to the transition regime. The white and grey areas are overlays of the referenced phase diagram obtained in Fig. 2.

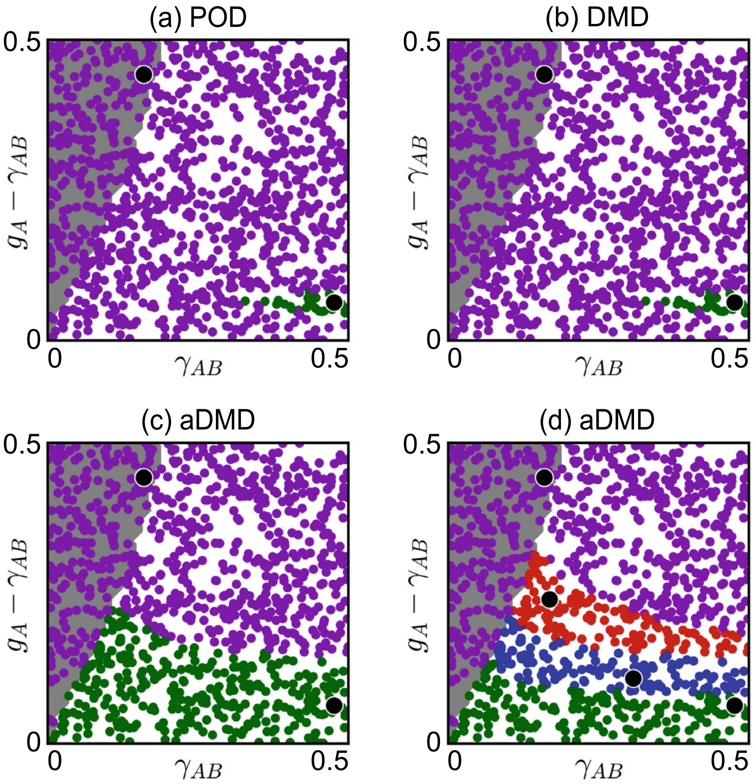

Fig. 4 **Representation classification using different decomposition methods**. Phase diagrams derived using a fixed library composed of two regimes (one in the oscillating and one in the non-oscillating phase), and with the bases in the library generated using the **a** POD, **b** DMD, **c** aDMD with $N_w = 25$. **d** Same as in panel (c) but with four regimes in the fixed library (one in the oscillating and three in the non-oscillating phase) The purple and green dots correspond respectively to the identified oscillating and non-oscillating regimes. The black dots represent the regimes used for the construction of the library. These black dots are located at $(\gamma_{AB}, g_A - \gamma_{AB}) = (0.16, 0.44)$ and $(0.48, 0.06)$ for panel (a), (b) and (c); and additionally at $(0.31, 0.11)$ and $(0.17, 0.24)$ for panel (d). The white and grey areas are overlays of the referenced phase diagram obtained in Fig. 2

Figure 4 shows the phase diagrams obtained from the different decomposition methods described in the previous section. In Fig. 4a, b and c, the purple (green) dots are the identified regime j^* [see Eq. (6)] from the oscillating (non-oscillating) regime. On one hand, Fig. 4a, b display the phase diagrams obtained from the POD and DMD method, respectively. As anticipated, the POD method fails to accurately reproduce the reference phase diagram [see Fig. 2] as the bases do not contain any temporal information: We observe that many time series are not correctly identified [Fig. 4a]. Similarly, the DMD method does not correctly identify the dynamics [Fig. 4b] as the bases from the DMD are similar to the POD bases. On the other hand, Fig. 4c illustrates that the aDMD (with $N_w = 25$) has better classification results: Less samples are being misidentified as the aDMD basis contains the temporal information of the dynamics.

While one might consider utilizing a different set of representative dynamics in the parameter space to construct the library $\mathcal{L}$ for potential improved results, such an approach would likely results in only marginal improvement of the classification. Instead, Fig. 4d demonstrates that redundantly increasing the number of representative dynamics in the library $\mathcal{L}$–in this case, four in total–yields much better results in correctly identifying the oscillating to the non-oscillating regime. In this context, the blue and red dots are the identified samples from the two new added representative dynamics: The identified oscillating and non-oscillating regimes now have a better fitting with the referenced phase diagram [Fig. 2], despite belonging to distinct regimes, namely having different index j^*. Therefore being able to identify the three colored for the oscillating regimes (green, blue, red) as corresponding to a single oscillating regime would give a more accurate diagram. This is the rationale of the methods, termed top-down and bottom-up adaptive classification, developed in the next sections: Adding redundant representative dynamics in the library $\mathcal{L}$ and being able to merge them corresponding to the oscillating or non-oscillating regime could potentially bring us closer to the desired phase diagram. The implications of these adaptive classification methods are two-fold: Firstly, prior knowledge of the system would not be needed, only measurement of its dynamics; secondly, the phase diagram would be constructed automatically from the samples.

4 Top-Down Adaptive Representation Classification

The top-down adaptive representation classification consist of adaptively refining the library initially composed of a redundant set of representative dynamics. This eliminates the manual process of selecting representative dynamics known from prior knowledge of the complex system considered. In practice, this top-down approach starts with many samples for the construction of the library, and then reduce the library size by merging some of them. From the previous section, this would mean that we merge the three phases in the non-oscillating region in Fig. 4d, and consider them as a single regime. Based on some measures in the decision process, this automated construction of the library thus removes the manual construction of the regimes.

The regimes are merged when considered to be equivalent, which is defined based on the dissimilarity between the subspace of different regimes. More precisely, the equivalence relation relied on the subspace alignment γ_{ij} that measures the dissimilarity between two subspaces i and j by projecting one subspace onto the other:

$$\gamma_{ij} := \frac{\|P_i P_j\|_F^2}{\|P_i\|_F \|P_j\|_F}, \tag{24}$$

with $\|\cdot\|_F$ the Frobenius norm of a matrix, $\|M\|_F := \sqrt{\sum_{ij} |M_{ij}|^2}$, and the projection operator defined as $P_j = \Phi_j \Phi_j^+$ [Eq. (7)]. Therefore, the regimes i and j are said to be equivalent, denoted by $i \sim j$, if the fraction of information retained after the projection onto each other, $\gamma_{ij} \in [0, 1]$, is high enough:

$$\gamma_{ij} > \gamma_{\text{th}}, \tag{25}$$

where $\gamma_{\text{th}} \in [0, 1]$ is a hyper-parameter deciding the threshold value for merging different regimes. Essentially, the relation Eq. (25) is numerically computed with a crucial emphasis on preserving the transitivity property of the equivalence relation, meaning that if $i \sim j$ and $j \sim k$ then $i \sim k$. The relation Eq. (25) is then indeed an equivalence relation because the reflexive $(i \sim i)$ and symmetric $(i \sim j \Rightarrow j \sim i)$ property of the relation is automatically satisfied from the definition of γ_{ij} [Eq. (24)]. Figure 5a illustrates the algorithm of the top-down approach. With an initial library $\mathcal{L}$ composed of a large number of representative regimes, the subspace alignment between all the bases is calculated, which can be viewed as being the (i, j) entries of a symmetric matrix γ [left of panel of Fig. 5a]. Then, the bases having a subspace alignment higher than γ_{th} are grouped together, while ensuring the transitivity relation is satisfied. Visually, this grouping procedure resemble a block diagonalization procedure of the subspace alignment matrix [middle panel of Fig. 5a]. Finally, for each of the blocks, one basis is selected and considered as the representative of the dynamical regime, which are plotted Fig. 5c.

In its core, the top-down representation classification entails in identifying the time series based on a comprehensive library of bases. It is only after this classification that equivalent identified regimes are merge using alignment subspace γ_{ij} and the equivalence relation specified in Eq. (25). Figure 5 shows the phase diagram resulting from the top-down algorithm with an initial library composed of $J = 60$ randomly chosen regimes. With this top-down approach, the resulted phase diagram is closed to the reference one [see Fig. 2] as we can see that the oscillating (purple dots) and non-oscillating (green dots) regimes can be distinguished. We can also see that a third regime is being distinguished from the oscillating and non-oscillating dynamics present in the literature. This is the transient regime (yellow dots) situated close to the $\gamma_{AB} = 0$ or $g_A - \gamma_{AB} = 0$ axis. Because we start looking at the dynamics after a time t_0, the transient regimes is an indication that a longer starting time and therefore longer simulation might be needed to consider them being in either one of the oscillating or non-oscillating regimes. In general, varying the parameter values also changes the relaxation times of the system, and the transient regime may then be the dominant regime. If that is the case, this would mean that the simulation has not run long enough to observe the main dynamical regimes.

The threshold parameter γ_{th} controlling the merging process is a critical quantity in the algorithm, as a low threshold γ_{th} will easily merge regimes while a high γ_{th} will still yield a relatively large size of the library as demonstrated in Fig. 5d. As a consequence, the two extreme cases will either consider all the dynamical regimes as being equivalent and identify all of them as being the same, or will not be able

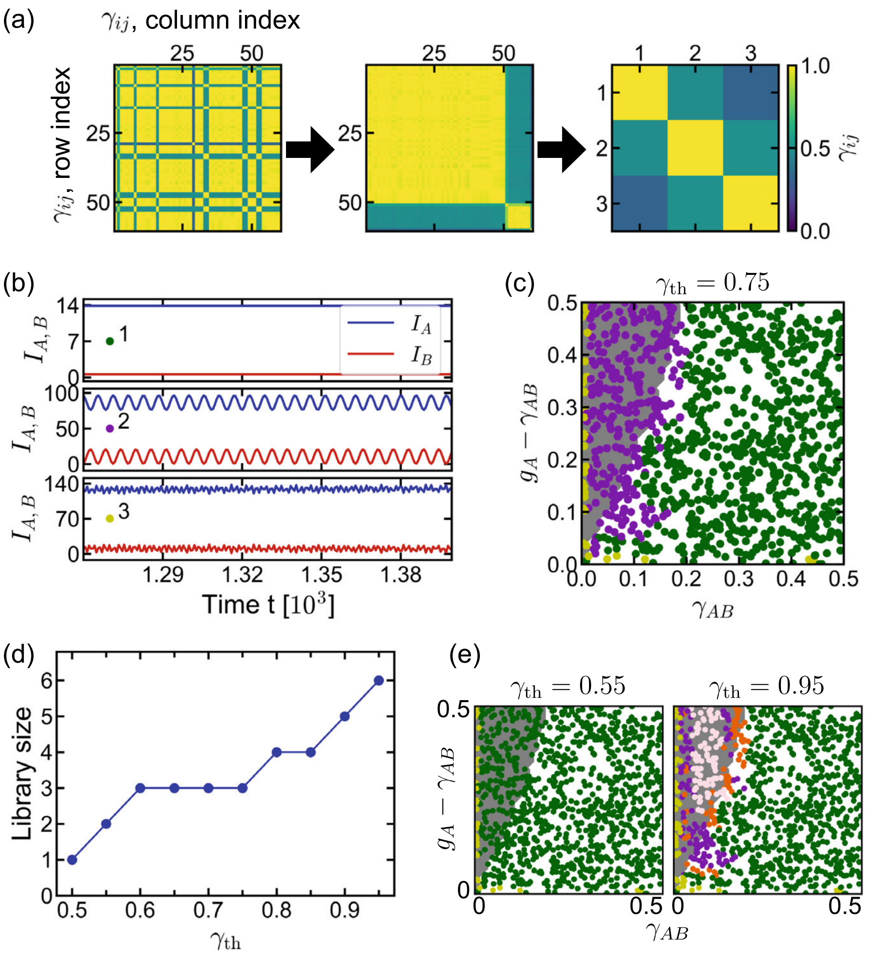

Fig. 5 **Principle of the top-down adaptive representation classification**. **a** Schematic of the top-down library generation: Starting with an initial library composed of $J = 60$ regimes, the subspace alignment matrix γ_{ij} is plotted (left panel), grouped into equivalent regimes with $\gamma_{\rm th} = 0.75$ (middle panel), then the subspace alignment matrix from the reduced library is plotted after the equivalent regimes are merged (right panel). **b** Representative time-evolution of the total intensity I_A (and I_B) of the A (and B) sublattice for the non-oscillating (top), oscillating (middle) topological lasing mode, and for the transient mode (bottom). **c** Phase diagram obtained using the top-down representation classification approach with an initial library composed of randomly chosen $J = 60$ regimes, with the hyper-parameter threshold $\gamma_{\rm th} = 0.75$. **d** Library size against the hyper-parameter threshold $\gamma_{\rm th}$, with an initial library composed of randomly chosen $J = 60$ regimes. **e** Phase diagrams obtained using the top-down classification approach with $\gamma_{\rm th} = 0.55$ (left) and $\gamma_{\rm th} = 0.95$ (right). The purple, green, yellow and orange dots correspond respectively to the identified oscillating, non-oscillating, transient and transition regimes. The white and grey areas are overlays of the referenced phase diagram obtained in Fig. 2

to see similarities between the time series, respectively. Therefore, the threshold is arbitrarily chosen based on the refinement of the desired library [see Fig. 5d, e]. Figure 5e shows examples of the phase diagram obtained with two different γ_{th} values. With $\gamma_{\text{th}} = 0.55$, the threshold value is too low as all the oscillating and non-oscillating regimes are being considered as equivalent, despite being able to distinguish the transient regimes with the others. However, using the same initial library but with a finer threshold value $\gamma_{\text{th}} = 0.95$, the top-down classification method is able to resolve six regimes grouped into four main regimes: The oscillating and non-oscillating known from the reference phase diagram [see Fig. 2], along with the regimes corresponding to the transient regime and to the transition between the two topological phases. Out of the six regimes, two are grouped into the oscillating phases, and two are grouped into the transient phases. The transition regime is different than the transient regimes, as the dynamics has already been reached the stationary regimes, and corresponds to the parameter values along the boundary between the two topological phases [see grey and white shaded areas in Fig. 5e]: therefore the method cannot correctly classify the regimes in this region as either oscillatory or non-oscillatory. Notably, this finer threshold provides distinct sets of modes in the oscillating parameter space region [see the purple and pink dots in Fig. 5e]. Those distinct oscillating modes were not present in the reference diagram [Fig. 2], and may have been overlooked as only the dynamics of the total intensity were considered in the literature [4].

Despite the success of the classification using the top-down approach, we can still see misclassification of the samples in the low γ_{AB} and low $g_A - \gamma_{AB}$ region (bottom-left region of the present phase diagram [Fig. 5b]), where some time series are interpreted as oscillating instead of non-oscillating regime. This is demonstrative of the limitation of this top-down automatic method where the initially constructed library may not encompass certain paths connecting similar bases. For example, the regimes i and k may not be similar enough to be considered as equivalent with respect to γ_{th}, but an "intermediate" regime j missing in the initial library and equivalent to both regimes i and k, i.e., $i \sim j$ and $j \sim k$, might make the regimes i and k equivalent thanks to the transitivity relation. This issue is dubbed here as the library having missing path, and the natural strategy to overcome this problem is to increase the initial library size to fill all the missing paths, as we will see in the next section.

5 Bottom-Up Adaptive Representation Classification

As an alternative approach to the top-down method, we propose the bottom-up classification which adaptively adds samples to the library on the fly. In practice, this bottom-up approach starts with few samples in the library and add bases to the library whenever the library is consider to be not good enough. The library is then reduced using the top-down approach to merge equivalent regimes. The key advantage of this bottom-up approach is the automatic construction of a library based on its quality. Therefore, the method does not rely on a more or less good choice of samples composing the library and has the potential to overcome the missing issue present in the top-down classification.

A sample is added to the library whenever the library cannot retrieve the dynamics of the given sample using its bases. This construction procedure is assessed via the maximal projection of the measurement onto the regimes' subspace ϵ:

$$\epsilon := \max_{j=1,\ldots,J} \frac{\|P_j y(t) - y(t)\|_2}{\|y(t)\|_2}, \tag{26}$$

with $\|\cdot\|_2$ the L_2-norm of a vector, and P_j is the projector defined in Eq. (7). In other words, the library is said to be good enough if the worst relative reconstruction error, ϵ, is low enough:

$$\epsilon < \epsilon_{\text{th}}, \tag{27}$$

where ϵ_{th} is the hyper-parameter deciding the threshold quality of the library. Figure 6a depicts the bottom-up approach algorithm. The library begins with a single sample, and is adaptively constructed based the relative reconstruction error [see left of panel Fig. 6a]. Once the library is established [see middle of panel Fig. 6a], the top-down approach is employed in order to merge equivalent regimes [see right of panel Fig. 6a]. Figure 6c shows the representative of the dynamical regimes after the top-down method is employed.

Fundamentally, the bottom-up representation classification scheme consists in initially classifying time series based on a given library or incorporating the sample into the library if the library is not good enough. Subsequently, the different phases are merged into equivalent regimes using the top-down method. Starting with a library composed of a single randomly chosen sample, the phase diagram obtained from the bottom-up classification is depicted in Fig. 6c. Comparable to the top-down approach shown in Fig. 5c, three distinct regimes are identified, corresponding to the oscillating (purple dots), non-oscillating (green dots) and transient (yellow dots) regimes. Notably, the phase diagram obtained from the bottom-up classification demonstrates an improved accuracy in identifying the regimes. The misclassifications previously observed of the oscillating and non-oscillating regimes, which were attributed to missing paths in the library, are now considerably reduced. Only few samples near the topological transition boundary are not correctly identified. Similarly to the top-down approach, the transient regimes indicates the need of a longer simulation time to correctly classify them.

Together with the hyper-parameter γ_{th}, the threshold hyper-parameter ϵ_{th} plays a crucial role in the bottom-up approach. Indeed, the decision of whether to add a sample to the library is a critical step in the algorithm. Setting a low threshold parameter will add too many samples, while a high ϵ_{th} will not add samples to the library at all, as shown in Fig. 6d. Therefore, the threshold value ϵ_{th} is, again, arbitrarily chosen based on the desired quality of the library [Fig. 6d, e]. Figure 6e illustrates two examples with different threshold parameter value, given $\gamma_{\text{th}} = 0.95$. Using $\epsilon_{\text{th}} = 0.05$, namely with a library that gives less than 5% of the reconstruction error of the measurement, the resulting phase diagram has four main regimes corresponding to the oscillating,

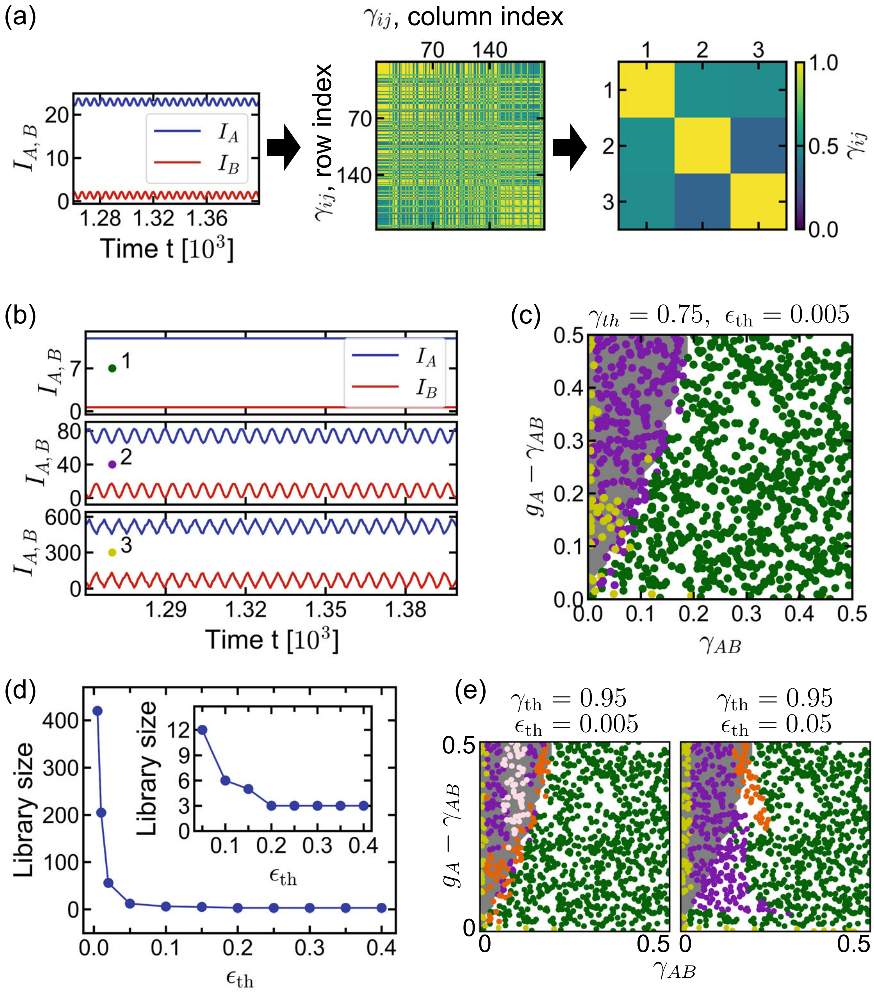

Fig. 6 **Principle of the bottom-up adaptive representation classification**. **a** Schematic of the bottom-up library generation: Starting with an initial library composed of a single randomly chosen regime (left panel), the library is increased according to the library quality where the subspace alignment matrix γ_{ij} of the final library is plotted (middle panel), then the subspace alignment matrix from the reduced library via the top-down approach is plotted (right panel). **b** Representative time-evolution of the total intensity I_A (and I_B) of the A (and B) sublattice for the non-oscillating (top), oscillating (middle) topological lasing mode, and for the transient mode (bottom). **c** Phase diagram obtained using the bottom-up representation classification approach with an initial library composed of single randomly chosen regime, with the hyper-parameters threshold $\epsilon_{\rm th} = 0.005$, $\gamma_{\rm th} = 0.75$. **d** Library size against the hyper-parameter threshold $\epsilon_{\rm th}$, with $\gamma_{\rm th} = 0.95$ and with an initial library composed of a single randomly chosen regime. **e** Phase diagrams obtained using the bottom-up classification approach with $\gamma_{\rm th} = 0.95$, and with $\epsilon_{\rm th} = 0.005$ (left) and $\epsilon_{\rm th} = 0.05$ (right). The purple, green, yellow and orange dots correspond respectively to the identified oscillating, non-oscillating, transient and transition regimes. The white and grey areas are overlays of the referenced phase diagram obtained in Fig. 2

non-oscillating, transition and transient regimes. However, there are instances of misidentification between the two oscillating and non-oscillating phases, likely due to missing paths in the obtained library, and suggesting that some samples need to be added in the library. With a better library quality, specifically setting $\epsilon_{\text{th}} = 0.005$, the missing paths are recovered, leading to a more accurate prediction of the topological phases in the resulting phase diagram: Both the oscillating and non-oscillating regimes are well positioned in their respective parameter space region. Moreover, a better library quality yields a more detailed phase diagram with the transition points not being able to be considered as oscillatory or non-oscillatory as this regime correspond to the transition boundary between the two topological phases, although some points are within the oscillatory regime. Significantly, the bottom-up representation classification distinguishes two oscillating modes [see the purple and pink dots in the right panel of Fig. 6e], instead of a single oscillating regime as shown in the reference diagram [see Fig. 2]. The identification of the distinct oscillating modes highlight the potential novel insights given by the data-driven classification method. In the context of this chapter, the classification method takes into account the complex values of the amplitudes of $x(t)$, rather than solely focusing on the total intensity of each sublattice A and B as done in Ref. [4, 13]. The use of complex valued here therefore enables a more detailed description of the dynamic pattern based on the entire lattice, incorporating information such as the relative phase difference of the sites or the absolute value of amplitudes.

6 Summary

In this chapter, we introduced an unsupervised machine-learning approach to identify topological phases of dynamic systems. In principle, this identification process is a representation classification, which finds a library that associates a finite number of labels for phases to parameters of a dynamic system. As an example, we explained how to draw the phase diagrams of the domain-wall-type SSH lattice with saturable gain.

As a mean to characterize the dynamic property, we introduced different decomposition methods including the POD, the DMD and the aDMD. By comparing the representation classification results using a fixed library based on the different methods, we observed that the aDMD works best for the domain-wall-type SSH lattice which has spatial and temporal variations in its field amplitudes.

In constructing the library, one can employ two schemes: top-down and bottom-up approaches that merge similar phases in a library or adaptively construct a library according to its quality, respectively. It is noteworthy that the libraries are constructed automatically and it does not require any detailed knowledge on the system. The libraries are optimized to represent all possible phases in a given parameter space by considering different measures defined on the libraries' bases. In the SSH laser example, we found the bottom-up adaptive scheme was the best approach to tackle the problem of drawing the phase diagram.

The bottom-up adaptive scheme can avoid pitfalls that can be encountered when using reverse engineering, such as missing paths in the equivalence relations, and can be used as a strategy to extend the method to more complex systems. While maybe not all phases might be identified on the first try, it is capable of clustering similar behaviour and gives a first classification of the different modes in the system. It should be complemented by a thorough analysis of these modes. Nonetheless, because of its different approach to drawing the phase diagram and its capability of clustering similar behaviour, reverse engineering holds the potential to find novel topological lasing modes, which could have been overlooked in other approaches.

Additionally, the machine-learning approach can be applied to many other dynamic systems composed of nonlinear resonators, for example, an array of quantum emitters and coupled mechanical resonators.

References

1. Bandres MA, Wittek S, Harari G, Parto M, Ren J, Segev M, Christodoulides DN, Khajavikhan M (2018) Topological insulator laser: experiments. Science 359(6381):eaar4005
2. Wu J, Ghosh S, Gan Y, Shi Y, Mandal S, Sun H, Zhang B, Liew TC, Su R, Xiong Q (2023) Higher-order topological polariton corner state lasing. Sci Adv 9(21):eadg4322
3. Longhi S, Kominis Y, Kovanis V (2018) Presence of temporal dynamical instabilities in topological insulator lasers. EPL 122(1):14004
4. Malzard S, Schomerus H (2018) Nonlinear mode competition and symmetry-protected power oscillations in topological lasers. New J Phys 20(6):063044
5. Yun J, Kim S, So S, Kim M, Rho J (2022) Deep learning for topological photonics. Adv Phys X 7(1):2046156 Mar
6. Araki H, Mizoguchi T, Hatsugai Y (2019) Phase diagram of a disordered higher-order topological insulator: a machine learning study. Phys Rev B 99(8):085406
7. Zhang P, Shen H, Zhai H (2018) Machine learning topological invariants with neural networks. Phys Rev Lett 120(6):066401
8. Peano V, Sapper F, Marquardt F (2021) Rapid exploration of topological band structures using deep learning. Phys Rev X 11(2):021052
9. Pedregosa F, Weiss R, Brucher M, Varoquaux G, Gramfort A, Michel V, Thirion B, Grisel O, Blondel M, Prettenhofer P, Weiss R, Dubourg V, Vanderplas J, Passos A, Cournapeau D, Brucher M, Perrot M, Duchesnay É (2011) Scikit-learn: machine learning in Python. J Mach Learn Res 12:2825–2830
10. Wang L (2016) Discovering phase transitions with unsupervised learning. Phys Rev B 94(19):195105
11. Scheurer MS, Slager R-J (2020) Unsupervised machine learning and band topology. Phys Rev Lett 124(22):226401
12. Su W-P, Schrieffer JR, Heeger AJ (1979) Solitons in polyacetylene. Phys Rev Lett 42(25):1698–1701
13. Malzard S, Cancellieri E, Schomerus H (2018) Topological dynamics and excitations in lasers and condensates with saturable gain or loss. Opt Express 26(17):22506
14. Bahari B, Ndao A, Vallini F, El Amili A, Fainman Y, Kanté B (2017) Nonreciprocal lasing in topological cavities of arbitrary geometries. Science 358(6363):636–640
15. Harari G, Bandres MA, Lumer Y, Rechtsman MC, Chong YD, Khajavikhan M, Christodoulides DN, Segev M (2018) Topological insulator laser: theory. Science 359(6381):eaar4003
16. Gong Y, Wong S, Bennett AJ, Huffaker DL, Oh SS (2020) Topological insulator laser using valley-Hall photonic crystals. ACS Photonics 7(8):2089–2097

17. Dikopoltsev A, Harder TH, Lustig E, Egorov OA, Beierlein J, Wolf A, Lumer Y, Emmerling M, Schneider C, Höfling S, Segev M, Klembt S (2021) Topological insulator vertical-cavity laser array. Science 373(6562):1514–1517
18. Yan Q, Xiaoyong H, Yulan F, Cuicui L, Fan C, Liu Q, Feng X, Sun Q, Gong Q (2021) Quantum topological photonics. Adv Opt Mater 9(15):2001739
19. Li Z, Luo X-W, Gu Q (2023) Topological on-chip lasers. APL Photonics 8(7):070901
20. Zhao H, Miao P, Teimourpour MH, Malzard S, El-Ganainy R, Schomerus H, Feng L (2018) Topological hybrid silicon microlasers. Nat Commun 9(1):981
21. Long-Hua W, Xiao H (2015) Scheme for achieving a topological photonic crystal by using dielectric material. Phys Rev Lett 114(22):223901 June
22. Wong S, Olthaus J, Bracht TK, Reiter DE, Oh SS (2023) A machine learning approach to drawing phase diagrams of topological lasing modes. Commun Phys 6(1):1–7
23. Proctor JL, Brunton SL, Brunton BW, Kutz JN (2014) Exploiting sparsity and equation-free architectures in complex systems. Eur Phys J Spec Top 223(13):2665–2684
24. Gavish M, Donoho DL (2014) The optimal hard threshold for singular values is $4/\sqrt{3}$. IEEE Trans Inf Theory 60(8):5040–5053
25. Schmid PJ (2010) Dynamic mode decomposition of numerical and experimental data. J Fluid Mech 656:5–28
26. Tu JH, Rowley CW, Luchtenburg DM, Brunton SL, Kutz JN (2014) On dynamic mode decomposition: theory and applications. J Comput Dyn 1(2):391–421
27. Kutz JN, Fu X, Brunton SL (2016) Multiresolution dynamic mode decomposition. SIAM J Appl Dyn Syst 15(2):713–735
28. Kramer B, Grover P, Boufounos P, Nabi S, Benosman M (2017) Sparse sensing and DMD-based identification of flow regimes and bifurcations in complex flows. SIAM J Appl Dyn Syst 16(2):1164–1196